Achievable Data Rate Improvement Analysis of a THz Multiple RIS-Assisted Factory System Based on Ray Tracing

Higo Thaian Pereira da Silva
Department of Electrical Engineering
Instituto Federal da Paraíba
João Pessoa, Brazil
higo.silva@ee.ufcg.edu.br

Ruan Delgado Gomes
Department of Electrical Engineering
Instituto Federal da Paraíba
João Pessoa, Brazil
ruan.gomes@ifpb.edu.br

Hugerles S. Silva
Department of Electrical Engineering
National Institute of Telecommunications
University of Brasília
Brasília, Brazil
hugerles.silva@unb.br

Rausley A. A. de Souza
National Institute of Telecommunications
Santa Rita do Sapucaí, Brazil
rausley@inatel.br

Felipe A. P. de Figueiredo
National Institute of Telecommunications
Santa Rita do Sapucaí, Brazil
felipe.figueiredo@inatel.br

***Abstract*—The application of reflective intelligent surfaces (RISs) combined with the vast bandwidth available in the THz spectrum band is an enabling technologies that can substantially enhance the performance of industrial networks in the sixth generation of wireless communications (6G). In this context, this work analyzes the performance improvement achieved by deploying multiple RISs in a system operating at 140 GHz in an indoor factory (InF) scenario. The analysis is based on ray tracing simulations using a geometric model representing an InF environment. The effects of specular reflection, diffraction, diffuse scattering, and atmospheric molecular absorption are considered in the propagation modeling. The performance of the networks is measured based on the achievable data rate (ADR), and the gain from using RISs is quantified by comparing it to the performance of a system without the RIS aid. According to the simulation results, the application of five RISs with 1000 reflecting elements promotes an increase of 4.1 bit/s/Hz in the average achievable rate when compared to the non-RIS-assisted system.**

***Index Terms*—Indoor factory, ray tracing, reflective intelligent surfaces, THz communications.**

I. Introduction

The key performance indicators (KPIs) forecast for the sixth generation (6G) of wireless communications indicate significant improvements compared to the established fifth generation (5G) networks. These KPIs suggest that 6G networks will provide up to a 50-fold increase in peak data rate and a reduction in latency to the millisecond level, while enabling a user density approximately 100 times greater than that of 5G networks [1]. Consequently, these projected performance levels establish new criteria for industrial applications, enabling the so-called Industry 5.0 [2], [3]. The technical objectives of Industry 5.0 fundamentally depend on developing of ultra-low latency and reliable communication (uLLRC) and ultra-high data rate (uHDR) services based on 6G technologies.

Among the main advances envisioned for 6G, the use of ultra-wide bandwidth in the terahertz (THz) bands is particularly notable, enabling high data rates in an indoor factory (InF) environment [2], [4]. This frequency band, established as the spectral range between 100 GHz and 10 THz, provides tens of GHz of available bandwidth, making it suitable for applications with high data rates, such as those required by uHDR services [4]. Another innovative 6G approach is the application of reflective intelligent surfaces (RISs) in industrial settings [5]. These surfaces provide control over electromagnetic scattering, significantly improving coverage in environments with a high likelihood of signal obstruction [6]. Communications in the THz band within InF environments benefit especially from using RISs, as links in this high-frequency band suffer from high path losses, low diffractive capacity, and high levels of atmospheric molecular absorption [7]. Furthermore, InF propagation scenarios naturally promote considerable signal blocking and shadowing levels due to the concentration of highly reflective and obstructive metallic equipment [8]. These challenges can be mitigated by strategically placing RISs, thereby enhancing overall coverage in industrial scenarios.

The effective implementation of 6G industrial networks fundamentally depends on accurately characterizing the wireless communication channel. In this context, ray tracing emerges as a powerful method, capable of describing the nature of electromagnetic propagation in the THz band, including particular phenomena of high frequencies, such as diffuse scattering [7], [9]. On the other hand, the simulation of RIS-assisted systems employing ray tracing has been the subject of research only recently, with few contributions due to the technological novelty of these surfaces [10]–[14]. However, to the best of the authors' knowledge, the coverage improvement in InF scenarios for systems operating in the THz band assisted

by RISs has not yet been adequately evaluated by applying realistic ray tracing modeling. Some of these works discuss the impact of RIS on coverage enhancement but are limited by their reliance on simplified simulation environments and lack of consideration for real-world factors such as diffraction and diffuse scattering effects.

This study aims to investigate the performance gain provided by multiple RISs considering a multiple-input single-output (MISO) system operating in the 140 GHz band within an InF environment [15]. This investigation is conducted through computational ray tracing simulations. The applied method is based on the shooting-and-bouncing rays (SBR) technique, which accounts for specular reflection, diffraction, diffuse scattering, and atmospheric molecular absorption to characterize the electromagnetic propagation of the direct channel. The RIS scattering is described based on the model presented in [16] and [6]. The performance of the simulated systems is evaluated based on the achievable data rate (ADR) and compared to that of an equivalent non-RIS-assisted system.

The remainder of this paper is organized as follows. Section II presents the system model, including the RIS scattering characterization and the calculation of the ADR. The basic principles of the applied ray tracing method and the InF propagation environment applied in the simulations are properly described in Section III. In Section IV, the simulation results are presented. Finally, Section V exposes the conclusions of the work.

II. System Model

The system studied in this work is illustrated in Fig. 1. It consists of an access point (AP) equipped with a uniform linear array (ULA) of N antenna elements that communicates with a single-antenna receiver (RX). The receiver represents an industrial network's sensor, actuator, device, or user equipment. The link between the AP and the receiver is determined by the direct channel (DC), characterized by the channel vector $\mathbf{d} \in \mathbb{C}^{N\times 1}$. The DC comprises the line-of-sight (LoS) component (when visibility conditions exist) and the scattered rays generated by the phenomena of specular reflection, diffraction, and diffuse scattering. The communication is assisted by K RISs strategically placed throughout the InF environment, in which each surface contains M reflecting elements. Consequently, a cascaded channel is formed by the AP-RIS and RIS-RX paths, defining the RIS-assisted channels (RACs). The phases of the passive elements of the RISs can be adjusted by the controller to appropriately modify the scattering of the incident wave. The RAC comprises only first-order interactions with the RISs, that is, direct incidences between the field transmitted by the AP and the surfaces. High-order interactions, such as scattering in the RISs caused by incidences of other scattered components or interactions between different RISs, are not considered [10].

It is assumed that each RIS element and the receiving points are in the far-field zone of the AP [10]. This assumption makes it sufficient to characterize the DC and the response between

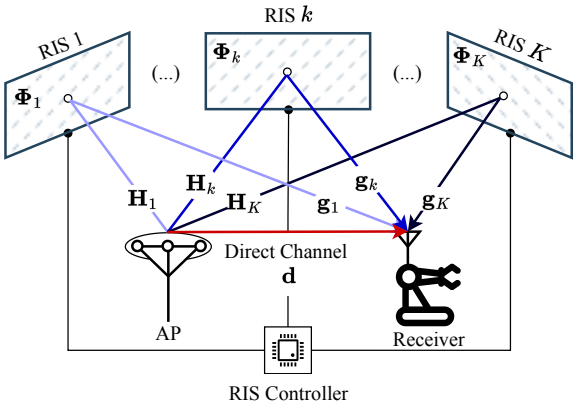

Fig. 1. System model.

the AP and a given RIS element by the ULA far-field response. However, for the InF scenario such as the one we studied, the receiver is not necessarily in the far-field zone of the RIS. This is due to the size of the surface, which can be relatively large, and to the physical space of the environment, which delimits short-range links. Therefore, a near-field characterization is necessary for RIS-RX links. Based on these considerations, the DC vector $\mathbf{d}$, composed by a superposition of N_r received rays, is expressed as [17]

$$\mathbf{d} = \sum_{l=1}^{N_\mathrm{r}} \sqrt{\bar{p}_l} e^{-j\bar{\varphi}_l} \mathbf{a}_{\mathrm{AP}}(\bar{\omega}_l), \tag{1}$$

in which $\bar{p}_l$, $\bar{\varphi}_l$ and $\bar{\omega}_l$ are the normalized power, phase, and spatial frequency related to the l-th received ray, respectively. The l-th spatial frequency term is expressed as $\bar{\omega}_l = \frac{2\pi}{\lambda}\delta_{\mathrm{AP}}\cos(\vartheta_l)$, in which λ is the wavelength, δ_{AP} is the ULA antenna spacing, and ϑ_l is the corresponding angle-of-arrival (in far-field conditions) of the received ray. The vector $\mathbf{a}_{\mathrm{AP}}(\cdot)$ is the far-field response of the AP array, generically calculated by

$$\mathbf{a}_{\mathrm{AP}}(\omega) = [1\ e^{-j\omega} \cdots e^{-j(n-1)\omega} \cdots e^{-j(N-1)\omega}]^T, \tag{2}$$

with ω denoting an arbitrary spatial frequency and $(\cdot)^T$ representing the transpose operation.

The cascaded RAC corresponding to the k-th RIS is composed by the AP-RIS channel $\mathbf{H}_k \in \mathbb{C}^{M\times N}$, the RIS phase response $\mathbf{\Phi}_k \in \mathbb{C}^{M\times 1}$, and the RIS-receiver channel, denoted as $\mathbf{g}_k \in \mathbb{C}^{M\times 1}$ [10]. The matrix $\mathbf{H}_k$ is written as

$$\mathbf{H}_k = [\mathbf{h}_{k,1}^T \cdots \mathbf{h}_{k,m}^T \cdots \mathbf{h}_{k,M}^T]^T, \tag{3}$$

in which $\mathbf{h}_{k,m} \in \mathbb{C}^{N\times 1}$ is the channel between the AP and the m-th reflecting element (with $m \in \{1, \cdots, M\}$) of the k-th RIS [10]. It is assumed that the RAC terms are subject to a sparse multipath composition, supported by two specific conditions. First, due to high path losses and significant shadowing in THz communications, the channel exhibits directive behavior, in which the direct incidence component contributes much more than the scattered components [18]. Second, the interaction of scattered components, such as

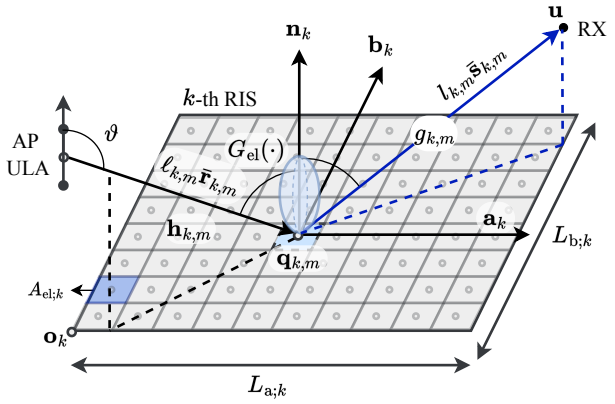

Fig. 2. Pictorial view of the RIS scattering geometry.

reflected rays, results in a negligible contribution to the RAC due to high scattering losses in RISs, which are proportional to the square of the product of the path lengths [6]. From these considerations, the channel vector $\mathbf{h}_{k,m}$ can be approximated by

$$\mathbf{h}_{k,m} = h_{k,m}\mathbf{a}_{\text{AP}}(\hat{\omega}_{k,m}), \tag{4}$$

in which $h_{k,m}$ and $\hat{\omega}_{k,m}$ are the complex gain and the spatial frequency related to the LoS incidence between the AP and the corresponding RIS's element. In turn, the channel vector between the k-th RIS and the receiver is given by $\mathbf{g}_k = [g_{k,1} \cdots g_{k,m} \cdots g_{k,M}]^T$, in which $g_{k,m}$ is the complex channel gain of the path between the m-th element of the corresponding RIS and the receiver. The behavior of $\mathbf{g}_k$ is not subject to a far-field approximation and depends on the near-field geometric characteristics of the scattering.

A. RIS Scattering Modeling

Each element of the RIS is modeled as a scattering unit. The geometry of this scattering is illustrated in Fig. 2. A given RIS is geometrically characterized by the set of features $\mathcal{S}_k = \{V_k, L_{\text{a};k}, L_{\text{b};k}, \mathbf{o}_k\}$ [10]. In this set, $V_k = (\mathbf{a}_k, \mathbf{b}_k, \mathbf{n}_k)$ is the orthonormal vector basis of reference of the k-th surface, in which $\mathbf{a}_k$ and $\mathbf{b}_k$ are vectors contained in the surface plane and $\mathbf{n}_k$ is a vector normal to the surface. In turn, $\mathbf{o}_k$ is a position vector that indicates the reference origin of the RIS geometry. In the directions indicated by vectors $\mathbf{a}_k$ and $\mathbf{b}_k$, the surface has lateral dimensions $L_{\text{a};k}$ and $L_{\text{b};k}$, respectively; resulting in a total area $A_{\text{RIS};k} = L_{\text{a};k} \times L_{\text{b};k}$. Consequently, each reflecting element has an area $A_{\text{el};k} = A_{\text{RIS};k}/M$.

Based on the far-field premise, the incident rays are emitted from the centroid of the AP ULA, which is located according to the position vector $\mathbf{t}$. These rays are directed to the reflecting elements, with a position defined by the vector $\mathbf{q}_{k,m}$, which indicates the center of the m-th element of the k-th RIS. Thus, the incident rays have incidence described by $\mathbf{r}_{k,m} \triangleq \mathbf{q}_{k,m} - \mathbf{t} = \ell_{k,m}\bar{\mathbf{r}}_{k,m}$, with $\ell_{k,m}$ denoting the incidence path length and $\bar{\mathbf{r}}_{k,m}$ representing the unitary direction vector. In turn, in the scattering path, the ray is directed from the RIS element to an arbitrary receiving point with a position indicated by $\mathbf{u}$. The scattering direction vector is expressed by $\mathbf{s}_{k,m} \triangleq \mathbf{u} - \mathbf{q}_{k,m} = l_{k,m}\bar{\mathbf{s}}_{k,m}$, in which $l_{k,m}$ is the scattering path length and $\bar{\mathbf{s}}_{k,m}$ is the corresponding unitary direction vector.

From the aforementioned geometric description, the channel coefficients $h_{k,m}$ and $g_{k,m}$ are expressed by [6], [16]

$$h_{k,m} = \sqrt{\frac{\rho_{\text{a};k,m} A_{\text{el;k}} G_{\text{el}}(\bar{\mathbf{r}}_{k,m}, \mathbf{n}_k)}{4\pi\ell_{k,m}^2}} e^{-j\frac{2\pi}{\lambda}\ell_{k,m}}, \tag{5}$$

and

$$g_{k,m} = \sqrt{\frac{\bar{\rho}_{\text{a};k,m} A_{\text{RX}} G_{\text{el}}(\bar{\mathbf{s}}_{k,m}, \mathbf{n}_k)}{4\pi l_{k,m}^2}} e^{-j\frac{2\pi}{\lambda}l_{k,m}}, \tag{6}$$

in which $\rho_{\text{a};k,m}$ and $\bar{\rho}_{\text{a};k,m}$ are the atmospheric molecular absorption factors in the incidence and scattering paths, $G_{\text{el}}(\cdot,\cdot)$ is the reflecting element radiation pattern and $A_{\text{RX}} = \lambda^2/4\pi$ is the receiver antenna aperture. The radiation pattern $G_{\text{el}}(\cdot,\cdot)$ depends on the angles of incidence and scattering and is generally expressed by [6], [16]

$$G_{\text{el}}(\mathbf{x}, \mathbf{n}_k) = G_0[(\mathbf{x} \cdot \mathbf{n}_k)]^{\left(\frac{G_0}{2}-1\right)} = G_0[\cos(\vartheta)]^{\left(\frac{G_0}{2}-1\right)}, \tag{7}$$

with $\mathbf{x} \cdot \mathbf{n}_k$ and ϑ representing the dot product and angle between the vectors $\mathbf{x}$ and $\mathbf{n}_k$, respectively, in which $\mathbf{x}$ is an arbitrary incidence/scattering vector; and G_0 symbolizing the peak radiation gain, directed perpendicularly to the surface.

B. Performance Analysis

The reflecting element of the RISs are associated with reflection coefficients, written as $\sigma_{k,m} = \alpha_{k,m}e^{j\Phi_{k,m}}$, where $\alpha_{k,m} = |\sigma_{k,m}| \leq 1$ is the corresponding magnitude and $\Phi_{k,m}$ is an adjustable phase term, used to control the scattering on the surface [19]. It is assumed that the magnitude is constant over the entire surface and independent of the corresponding phase, *i.e.*, $\alpha_{k,m} = \bar{\alpha}_k$, $\forall m \in \{1, \cdots, M\}$. Furthermore, it is supposed that the phase of the elements can be configured continuously in the interval $[0, 2\pi]$. Thus, the k-th RIS response matrix is defined as [18]

$$\mathbf{\Phi}_k = \alpha_k \text{diag}(\boldsymbol{\phi}_k), \tag{8}$$

with $\text{diag}(\cdot)$ representing the diagonal operator and $\boldsymbol{\phi}_k = [e^{j\Phi_{k,1}} \cdots e^{j\Phi_{k,M}}]^T$. In this case, the narrowband received signal at the receiver is expressed by the composition of the DC and the K RACs, that is,

$$r = \sqrt{P}\left(\sum_{k=1}^{K} \alpha_k \boldsymbol{\phi}_k^T \mathbf{V}_k + \mathbf{d}^T\right)\mathbf{w}s + n_0, \tag{9}$$

in which P is the transmitted power, $\mathbf{w} \in \mathbb{C}^{N\times 1}$ is the precoding vector applied by the AP, s is the unit power transmitted signal and n_0, is the zero mean additive white Gaussian noise (AWGN) at the receiver with variance σ_{n}^2. In (9), the term $\mathbf{V}_k = \text{diag}(\mathbf{g}_k)\mathbf{H}_k \in \mathbb{C}^{M\times N}$ is the cascaded channel matrix [17]. The signal-to-noise ratio (SNR) experienced by the receiver is calculated by [17]

$$\Upsilon = \frac{P}{\sigma_{\text{n}}^2}\left|\left(\sum_{k=1}^{K} \alpha_k \boldsymbol{\phi}_k^T \mathbf{V}_k + \mathbf{d}^T\right)\mathbf{w}\right|^2. \tag{10}$$

Assuming a simplified genie-aided case with perfect knowledge of the channels, the AP applies a maximum ratio combining (MRC) precoding to design the vector $\mathbf{w}$ [17], [19]. In turn, a low-complexity design is applied to the RIS phases $\Phi_{k,m}$ [19], resulting in

$$\Phi_{k,m} = [\boldsymbol{\phi}_k]_m = \exp\left(-\angle[\mathbf{z}_k]_m\right), \tag{11}$$

in which $\mathbf{z}_k = \mathbf{V}_k\mathbf{d}^\star \in \mathbb{C}^{M\times 1}$, with $(\cdot)^\star$ representing the conjugation of a complex-valued matrix; and $\angle(\cdot)$ denotes the phase of a complex number. The beamformer designed by (11) ensures that the RACs' rays add up coherently at the receiver [19]. Based on the these premises, the ADR at the receiver, expressed in bit/s/Hz, is given by [17]

$$R = \log_2\left(1 + \frac{P}{\sigma_{\text{n}}^2}\left\|\sum_{k=1}^{K}\alpha_k\boldsymbol{\phi}_k^T\mathbf{V}_k + \mathbf{d}^T\right\|^2\right), \tag{12}$$

in which $\|\cdot\|$ represents the Euclidean norm of a vector.

III. Ray Tracing Modeling

This section presents the basic principles of ray tracing that are considered according to the SBR method. For definition purposes, a ray is abstractly represented as a set $\mathcal{R}$, comprising elements of a line segment $\mathbf{x}_\mathcal{R}$ and an electric field vector $\mathbf{E}_\mathcal{R}$. The line segment $\mathbf{x}_\mathcal{R}$ describes the propagation path and is defined as $\mathbf{x}_\mathcal{R} = \mathbf{o}_\mathcal{R} + \ell_\mathcal{R}\mathbf{r}_\mathcal{R}$, in which $\mathbf{o}_\mathcal{R}$ is the ray path origin, $\ell_\mathcal{R}$ is the path length, and $\mathbf{r}_\mathcal{R}$ is the unitary norm direction vector. The initial characteristics of the ray are established during the transmission stage, which is responsible for emitting rays from a specified source point. The initial source point is defined as the centroid coordinate of the AP's ULA. During this stage, rays are emitted with an approximately uniform angular distribution, ensuring that the transmission from the AP behaves as an isotropic source, meaning it exhibits no angular bias. To achieve this, the icosahedron method is applied, where the faces of a regular icosahedron are iteratively subdivided into facets to generate a dense mesh of vertices [20]. These vertices form an icosphere centered on the transmission point and indicate the directions of the rays. The number of rays emitted during the transmission stage is determined by [21]

$$N_\mathcal{R} = 10N_{\text{fd}}^2 + 2, \tag{13}$$

in which N_{fd} is the number of segments applied in the icosahedron subdivision process. The average angular separation between adjacent rays, which determines the spatial resolution of the ray tracing simulations, is given by [22]

$$\Delta\theta \approx \frac{1.205 \text{ rad}}{N_{\text{fd}}} \approx \frac{69^\circ}{N_{\text{fd}}}. \tag{14}$$

Subsequent to the transmission of the ray $\mathcal{R}$, the tracing step follows. In this step, the length $\ell_\mathcal{R}$ is interactively incremented along the space following the uniform spatial division methodology described in [23], [24]. At each incremental step, the proximity of the ray to any object in the propagation environment is assessed. If the ray is near an object, ray-object intersection tests are conducted. Upon detecting an intersection, the ray is updated according to the principles of specular reflection. This update modifies the $\mathbf{x}_\mathcal{R}$ and $\mathbf{E}_\mathcal{R}$ vectors based on the reflective interaction. Then, the tracing process is restarted with the updated ray. This procedure is repeated recursively until the maximum number of reflections is reached. The interactions between rays and objects are also responsible for generating sources used to characterize the diffraction and diffuse scattering phenomena [7].

After the tracing phase, the ray reception phase begins. For any receiver at a well-defined position, whether a given ray contributes to the link is determined through ray-sphere intersection tests. If a ray approaches a receiving point, a sphere centered on that point is defined. The contribution is considered if the ray intersects the sphere. The radius of the reception sphere is calculated by [25]

$$r_{\text{rx}} = \frac{1}{\sqrt{3}}\ell_{\text{R};T}\Delta\theta, \tag{15}$$

in which $\ell_{\mathcal{R};\text{T}}$ is the total unfolded path length. The radius expressed in (15) is designed to minimize the reception of multiple rays corresponding to the same wavefront, a problem known as double counting [25]. Although this approach reduces the incidence of double counting, there remains a probability that these events may still occur. To completely eliminate this issue, the characteristic sequence method is applied [26]. After all $N_\mathcal{R}$ rays transmitted by the AP have been processed, the subsequent steps involve the transmission of diffraction and diffuse scattering rays, based on the uniform theory of diffraction (UTD) [27], [28] and Beckmann-Kirchhoff theory [9], [29], respectively.

Considering the effects of specular reflection, diffraction, diffuse scattering, and atmospheric molecular absorption, the normalized power of an arbitrary received ray is generically expressed by

$$p_{\text{r}} = \frac{\lambda^2}{(4\pi)^2}A_{\text{fs}}\rho_{\text{t}}\prod_i\left(A_{\text{re}}\Gamma_i^2\rho_{\text{ds};i}^2\right)\prod_j\left(A_{\text{d};j}D_j^2\right)\prod_k\left(A_{\text{ds};j}\zeta_k^2\right). \tag{16}$$

In (16), A_{fs} is the free-space divergence factor and $\rho_{\text{t}} = \rho_{\text{p}}\rho_{\text{a}}$, in which ρ_{p} is the polarization mismatch loss and ρ_{a} is the atmospheric molecular absorption attenuation by dry air and water vapor, calculated applying the model presented in the recommendation ITU-R P.676 [30]. The factors Γ_i and D_j are the reflection and diffraction losses based on the Fresnel coefficients and the UTD [27], [28], respectively. In turn, ζ_k is the diffuse scattering loss based on the Beckmann-Kirchhoff theory [9]. Finally, A_{re}, A_{d}, and A_{ds} are the divergence factors related to the reflection, diffraction, and diffuse scattering, respectively. It is important to emphasize that the ray tracing methodology described in this section is suitable for characterizing of the DC. The determination of RACs should be treated separately, following the specificities of the scattering by RISs [6], [16], as presented in Section II-A.

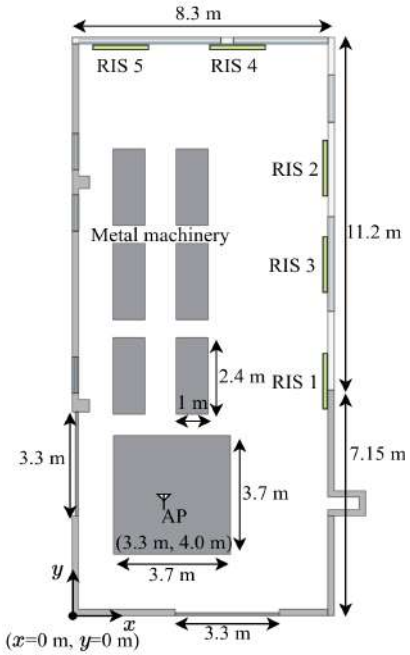

Fig. 3. Geometric description of the propagation scenario. This environment is based on a real industrial warehouse located in the technological hub of the IFPB in João Pessoa, Brazil.

A. Environment Characterization

The propagation environment model used in the ray tracing simulations is based on a real industrial warehouse located in the technological hub of the Federal Institute of Paraíba (IFPB) in João Pessoa, Brazil. As depicted in Fig. 3, this environment covers an area of 8.3 m×18.35 m, with a ceiling height of 3 m. The warehouse is enclosed by concrete and plaster walls, each with a thickness of 0.2 m, and features glass windows. Inside, the space contains various machines and equipment, represented as metal blocks with a height of 1.8 m. The metal machines occupy 19% of the scenario area. The material properties in the environment are extrapolated using the model specified in the International Telecommunication Union (ITU) recommendation P.2040 [31]. Additionally, the effective roughness of the materials, an important parameter for characterizing diffuse scattering, is determined based on [29], [32]. Five RISs are distributed along the environment, each with a specific identifying index. All surfaces have the same dimensions of 2 m×1 m ($A_{\text{RIS;k}} = 2$ m^2), with the centroid of the rectangular face positioned at a height of 1.5 m. The entire propagation environment is segmented into a grid of square microregions, in which virtual receivers are positioned at their centers at a height h_{rx}. Virtual receivers placed internally to some object (walls or furniture) are discarded.

IV. Simulation Results

The ray tracing simulations are conducted using the environment discussed in Section III-A, with an AP located at coordinates (4.0 m, 3.3 m), as shown in Fig. 3. The AP is positioned at a height of $h_{\text{AP}} = 3$ m (fixed to the ceiling of the InF environment) and integrates an ULA with $N = 32$ antenna elements. The receivers are distributed across the reception grid at a height of $h_{\text{rx}} = 1.5$ m. The system operates at 140 GHz with a transmitted power of 0 dBm, while the noise power is -94 dBm. The simulation is configured with an angular difference between adjacent rays of $\Delta\theta = 0.067°$ ($N_{\text{fd}} = 1024$), with a maximum of six reflections per path. Only first-order diffractions are considered. Additionally, all RISs in the environment are assumed to share the same operating characteristics. The RISs have elements with directivity gains of $G_0 = 8$ (9 dBi) and reflection losses of $\alpha_k = 0.8$. The specifications of the ray tracing simulations are summarized in Table I. To evaluate different configurations of RIS-assisted systems, five simulation cases are considered. For each case, the number of active RISs varies. In the k-th simulation case, denoted as C_k, with $k \leq 5$; the RISs with indices in the set $S_k = \{1, \cdots, k\}$ are activated (see Fig. 3).

TABLE I
Specifications of Ray Tracing Simulations.

Parameter	Value
AP coordinates	(4.0 m, 3.3 m)
AP height – h_{AP}	3.0 m
Number of antenna elements – N	32
Receiver height – h_{rx}	1.5 m
Carrier frequency	140 GHz
Transmitted power – P	0 dBm
Noise variance – σ_{n}	-94 dBm
Angular resolution – $\Delta\theta$	0.067°
Maximum number of reflections	6
RIS elements directivity gain – G_0	8 (9 dBi)
RIS elements reflection losses – α_k	0.8

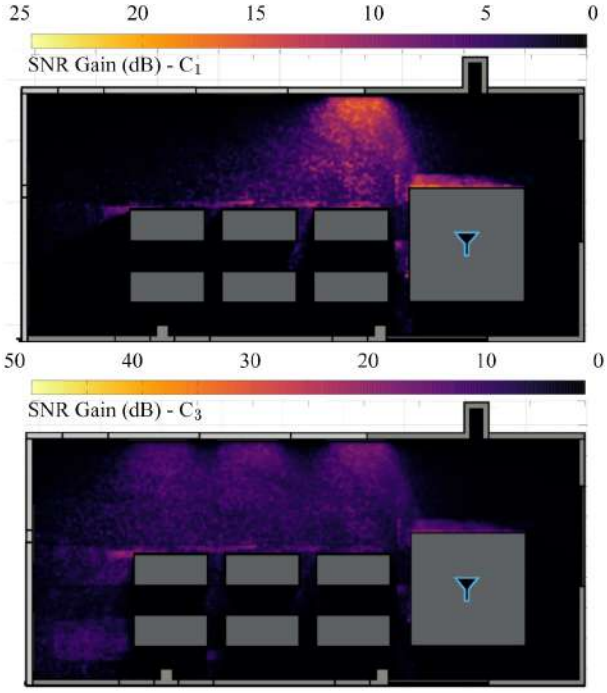

Fig. 4. Heat maps of the point-to-point SNR gain provided by the RISs in simulation cases C_1 and C_3 considering $M = 100$.

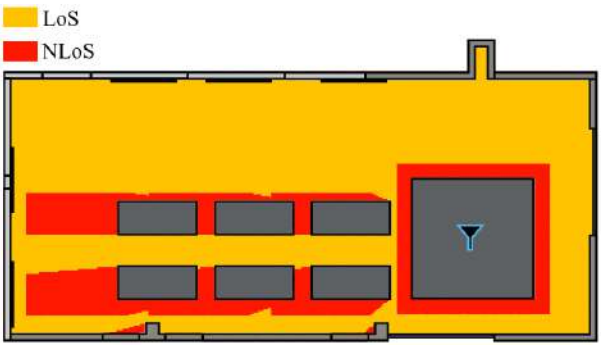

Fig. 5. Map of LoS conditions related to the AP position obtained from ray tracing simulations.

TABLE II
SUMMARY OF THE RAY TRACING SIMULATIONS RESULTS.

M	Link Type	Achievable Rate (bit/s/Hz)				
		C_1	C_2	C_3	C_4	C_5
100	Global	4.04	4.40	4.63	5.23	5.83
	LoS	4.44	4.81	5.07	5.45	6.06
	NLoS	2.61	2.95	3.08	4.43	5.01
1000	Global	4.70	5.55	5.93	6.85	7.69
	LoS	5.10	5.94	6.37	6.99	7.88
	NLoS	3.24	4.15	4.39	6.36	7.05

The simulation results presented in this section represent point-to-point links, with a fixed AP and receiver positioned within the coverage area. The precoding and beamforming methodology described in Subsection II-B is specific to individual links. Fig. 4 presents heat maps generated via ray tracing simulations, illustrating the point-to-point SNR gains achieved by the RIS in scenarios C_1 (with RIS 1 active) and C_3 (with RIS 1, 2, and 3 active) for $M = 100$. The SNR gain is quantified as the ratio of the RIS-assisted SNR to the non-RIS-assisted SNR. For reference on the link conditions at each position, refer to Fig. 5, which maps the LoS conditions relative to the AP. The heat maps in Fig. 4 demonstrate a radiation pattern that forms perpendicularly to the RISs, attributed to the elements' directivity, which peaks along the normal vector to the surfaces. Furthermore, the emergence of zones with significant SNR gain is noticeable around the object contours, particularly in regions experiencing obstructions (see Fig. 5). This effect is primarily due to the substantial impact of RISs in obstructed regions, which typically suffer from high path losses caused by the blockage from the metal machinery present in the environment.

The ADR experienced by the receiver is characterized by applying the absolute SNR results ino (12). Table II summarizes of the average ADR for the considered simulation cases, with $M \in \{100, 1000\}$. The values in this table are segmented by link type, *i.e.*, LoS links or non-line-of-sight (NLoS) links. Additionally, global statistics that consider both link types are presented. For benchmarking, simulations were conducted in a non-RIS-assisted system, resulting in average ADRs of 3.59 bit/s/Hz, 3.98 bit/s/Hz, and 2.21 bit/s/Hz for the global calculation, LoS links, and NLoS links, respectively.

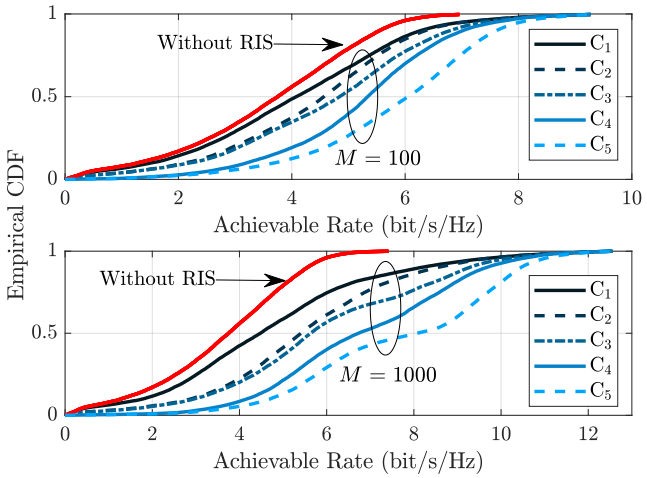

Fig. 6. Empirical CDF curves of the ADR obtained from the ray tracing simulations considering $M \in \{100, 1000\}$.

Based on the results presented in Table II, an expected increase in the average data rate is observed with the rise in the number of operating RISs in the system. Specifically, for LoS links, the average data rate increases from 4.44 bit/s/Hz in case C_1 to 6.06 bit/s/Hz in case C_5 when RISs with $M = 100$ elements are used. Additionally, the impact of the number of elements on these results can be evaluated. In case C_3 for LoS links, the average rate rises from 5.07 bit/s/Hz to 6.37 bit/s/Hz when RISs with $M = 1000$ elements are utilized instead of $M = 100$ elements, indicating an increase of 1.3 bit/s/Hz in the average rate.

Furthermore, the relative gain in average rate due to applying RISs is more significant in NLoS links. In InF environments operating at THz frequencies, the level of blockage by metallic objects and natural path losses are severe, leading to highly shadowed NLoS links. In these scenarios, RISs serve as an efficient solution to ensure coverage. For instance, in the NLoS case without RISs, the average calculated rate is 2.21 bit/s/Hz. Implementing $k = 4$ RISs with 1000 elements results in an average rate gain of 4.15 bit/s/Hz, corresponding to an improvement of 187% in performance.

Fig. 6 presents the empirical cumulative distribution functions (CDF) of the global ADR results obtained from the ray tracing simulations, considering $M = \{100, 1000\}$. Considering the 50-th percentile (median) of the non-RIS-aided system as a reference, which has a value of 3.7 bit/s/Hz, it is evident that the application of multiple RISs significantly improves coverage. Specifically, in the case of C_5 with 100-element RISs, the median increases to approximately 6 bit/s/Hz. On the other hand, by using a 1000-element RISs, the same percentile rises to approximately 8 bit/s/Hz, indicating that 50% of the entire propagation environment can achieve a higher rate than this value.

Fig. 7 shows the curves of the average ADRs varying the number of RIS elements in the simulation cases for LoS and NLoS links. The result for the system without RIS assistance is also presented as a benchmark. From these results, it is

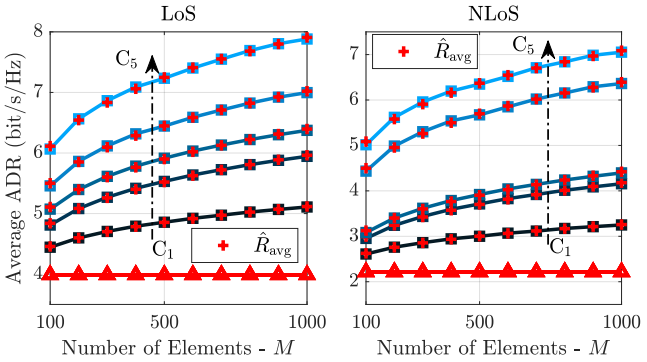

Fig. 7. Curves of average ADR values as a function of the number of elements M for the considered simulation cases.

TABLE III
VALUES μ_1 AND μ_2 FOR THE DIFFERENT SIMULATION CASES.

Simulation Case		Parameter μ_1 (bit/s/Hz)	Parameter μ_2
C_1	LoS	0.0810	0.3813
	NLoS	0.0631	0.4060
C_2	LoS	0.1578	0.3658
	NLoS	0.1214	0.4029
C_3	LoS	0.2421	0.3325
	NLoS	0.1544	0.3849
C_4	LoS	0.3759	0.3022
	NLoS	0.6824	0.2622
C_5	LoS	0.6246	0.2659
	NLoS	0.9961	0.2297

observed that these curves can be numerically fitted according to the expression

$$\hat{R}_{\text{avg}}(M) = \mu_1 M^{\mu_2} + \tilde{R}_{\text{avg};0}, \tag{17}$$

in which μ_1 and μ_2 are fitting parameters related to the growth rate of $\hat{R}_{\text{avg}}$ and $\tilde{R}_{\text{avg};0}$ is the average ADR in the non-RIS-assisted system. Note that (17) is not scalable for any value of M, which would result in an infinite average rate when $M \to \infty$, not satisfying the practical physical limits of RIS in the near field [33]. Therefore, this expression is valid in the context addressed in this work. The values of μ_1 and μ_2 for the different simulated cases are shown in Table III.

The results in Table III show that μ_1 increases as the number of RISs in the system increases, while the μ_2 parameter decreases as k increases. This suggests that although the average rate improves with more RISs, the gain is limited. It may be more beneficial to use fewer surfaces with a larger number of elements. Additionally, comparing the μ_2 parameters of LoS and NLoS channels for the same system configuration reveals that the $\hat{R}_{\text{avg}}(M)$ functions have higher powers in NLoS links. This indicates that obstructed channels benefit more from an increased number of RIS elements, which is particularly important for InF scenarios in THz environments with high shadowing levels. Thus, multiple RISs are a key approach to mitigating high path losses and homogenizing coverage in InF systems.

V. CONCLUSIONS

This study has analyzed the performance gains in terms of achievable data rate (ADR) promoted by multiple reflective intelligent surfaces (RIS) in a system operating at 140 GHz within an indoor factory (InF) scenario, using ray tracing simulations. The results have shown that deploying five RISs with 100 elements each achieves an average data rate of 6.06 bit/s/Hz, an increase of 2.08 bit/s/Hz compared to a system without RISs. Additionally, the gain in the average rate is more significant in non-line-of-sight (NLoS) links. For instance, with four RISs of 1000 elements each, there has been a 187% improvement in the average ADR of NLoS links. Furthermore, a power expression enabled the numerical characterization of the average ADR's variation rate concerning the number of RIS elements. These findings demonstrate that applying RISs in InF environments effectively enhances performance and standardizes coverage, particularly in THz band applications. As future work, the authors plan to assess the benefits of RISs, taking into account their technical limitations, including inaccuracies in channel state information, constraints in phase control of the elements, and the interdependence between the magnitude and phase of the surface elements' reflection coefficients.

ACKNOWLEDGMENT

The authors thank CNPq (305536/2021-4), FAPESQ, PPGEE/IFPB, and the IFPB Innovation Hub. This work was partially supported by Rede Nacional de Ensino e Pesquisa (RNP), with resources from Ministério da Ciência, Tecnologia e Inovações (MCTIC), under the Brazil 6G Project of the Radiocommunication Reference Center (Centro de Referência em Radiocomunicações (CRR)) of the National Institute of Telecommunications (Instituto Nacional de Telecomunicações (Inatel)), Brazil, under Grant 01245.010604/2020-14, by CNPq (Grant References 311470/2021-1 and 403827/2021-3), by the projects XGM-AFCCT-2024-2-5-1 and XGM-FCRH-2024-2-1-1 supported by xGMobile – EMBRAPII-Inatel Competence Center on 5G and 6G Networks, with financial resources from the PPI IoT/Manufatura 4.0 from MCTI grant number 052/2023, signed with EMBRAPII, and by Fapemig (PPE-00124-23)

REFERENCES

[1] M. Z. Chowdhury, M. Shahjalal, S. Ahmed, and Y. M. Jang, "6G Wireless Communication Systems: Applications, Requirements, Technologies, Challenges, and Research Directions," *IEEE Open Journal of the Communications Society*, vol. 1, pp. 957–975, 2020.

[2] A. Hazra, A. Munusamy, M. Adhikari, L. K. Awasthi, and V. P, "6G-Enabled Ultra-Reliable Low Latency Communication for Industry 5.0: Challenges and Future Directions," *IEEE Communications Standards Magazine*, vol. 8, no. 2, pp. 36–42, 2024.

[3] R. Tallat, A. Hawbani, X. Wang, A. Al-Dubai, L. Zhao, Z. Liu, G. Min, A. Y. Zomaya, and S. Hamood Alsamhi, "Navigating Industry 5.0: A Survey of Key Enabling Technologies, Trends, Challenges, and Opportunities," *IEEE Communications Surveys Tutorials*, vol. 26, no. 2, pp. 1080–1126, 2024.

[4] C. Chaccour, M. N. Soorki, W. Saad, M. Bennis, P. Popovski, and M. Debbah, "Seven Defining Features of Terahertz (THz) Wireless Systems: A Fellowship of Communication and Sensing," *IEEE Communications Surveys Tutorials*, vol. 24, no. 2, pp. 967–993, 2022.

[5] H. Ren, K. Wang, and C. Pan, "Intelligent Reflecting Surface-Aided URLLC in a Factory Automation Scenario," *IEEE Transactions on Communications*, vol. 70, no. 1, pp. 707–723, 2022.

[6] W. Tang, X. Chen, M. Z. Chen, J. Y. Dai, Y. Han, M. D. Renzo, S. Jin, Q. Cheng, and T. J. Cui, "Path Loss Modeling and Measurements for Reconfigurable Intelligent Surfaces in the Millimeter-Wave Frequency Band," *IEEE Transactions on Communications*, vol. 70, no. 9, pp. 6259–6276, 2022.

[7] H. T. P. da Silva, H. S. Silva, M. S. Alencar, W. J. L. Queiroz, and U. S. Dias, "Characterization of Large-Scale Parameters in Indoor THz Channels Applying the Ray Tracing Method," in *2022 Workshop on Communication Networks and Power Systems (WCNPS)*, 2022, pp. 1–6.

[8] T. Jiang, J. Zhang, P. Tang, L. Tian, Y. Zheng, J. Dou, H. Asplund, L. Raschkowski, R. D'Errico, and T. Jämsä, "3GPP Standardized 5G Channel Model for IIoT Scenarios: A Survey," *IEEE Internet of Things Journal*, vol. 8, no. 11, pp. 8799–8815, 2021.

[9] F. Sheikh, Y. Gao, and T. Kaiser, "A Study of Diffuse Scattering in Massive MIMO Channels at Terahertz Frequencies," *IEEE Transactions on Antennas and Propagation*, vol. 68, no. 2, pp. 997–1008, 2020.

[10] H. T. P. Da Silva, M. S. De Alencar, W. J. Lira Queiroz, and H. S. Silva, "Coverage Probability Analysis of a RIS-Assisted THz Indoor System Based on Ray Tracing Simulations," in *2023 IEEE Latin-American Conference on Communications (LATINCOM)*, 2023, pp. 1–6.

[11] E. M. Vitucci, M. Albani, S. Kodra, M. Barbiroli, and V. Degli-Esposti, "An Efficient Ray-Based Modeling Approach for Scattering From Reconfigurable Intelligent Surfaces," *IEEE Transactions on Antennas and Propagation*, vol. 72, no. 3, pp. 2673–2685, 2024.

[12] J. Huang, C.-X. Wang, Y. Sun, J. Huang, and F.-C. Zheng, "A Novel Ray Tracing Based 6G RIS Wireless Channel Model and RIS Deployment Studies in Indoor Scenarios," in *2022 IEEE 33rd Annual International Symposium on Personal, Indoor and Mobile Radio Communications (PIMRC)*, 2022, pp. 884–889.

[13] J. Huang, C.-X. Wang, S. Yang, Y. Wang, Y. Xu, Y. Sun, J. Huang, and F.-C. Zheng, "Ray Tracing Based 6G RIS-Assisted MIMO Channel Modeling and Verification," in *2023 IEEE/CIC International Conference on Communications in China (ICCC)*, 2023, pp. 1–6.

[14] A. Tarozzi, E. M. Vitucci, F. Fuschini, and R. Verdone, "Metasurfaces as 6G Enabling Technology: A discussion on RIS applicability to Industrial IoT scenarios," in *2024 IEEE International Workshop on Metrology for Industry 4.0 IoT*, 2024, pp. 377–382.

[15] S. Ju and T. S. Rappaport, "142 GHz Multipath Propagation Measurements and Path Loss Channel Modeling in Factory Buildings," in *ICC 2023 - IEEE International Conference on Communications*, 2023, pp. 5048–5053.

[16] W. Tang, M. Z. Chen, X. Chen, J. Y. Dai, Y. Han, M. Di Renzo, Y. Zeng, S. Jin, Q. Cheng, and T. J. Cui, "Wireless Communications With Reconfigurable Intelligent Surface: Path Loss Modeling and Experimental Measurement," *IEEE Transactions on Wireless Communications*, vol. 20, no. 1, pp. 421–439, 2021.

[17] N. K. Kundu and M. R. McKay, "Channel Estimation for Reconfigurable Intelligent Surface Aided MISO Communications: From LMMSE to Deep Learning Solutions," *IEEE Open Journal of the Communications Society*, vol. 2, pp. 471–487, 2021.

[18] P. Wang, J. Fang, X. Yuan, Z. Chen, and H. Li, "Intelligent Reflecting Surface-Assisted Millimeter Wave Communications: Joint Active and Passive Precoding Design," *IEEE Transactions on Vehicular Technology*, vol. 69, no. 12, pp. 14 960–14 973, 2020.

[19] D. Mishra and H. Johansson, "Channel Estimation and Low-complexity Beamforming Design for Passive Intelligent Surface Assisted MISO Wireless Energy Transfer," in *ICASSP 2019 - 2019 IEEE International Conference on Acoustics, Speech and Signal Processing (ICASSP)*, 2019, pp. 4659–4663.

[20] S. Shikhantsov, A. Thielens, G. Vermeeren, E. Tanghe, P. Demeester, L. Martens, G. Torfs, and W. Joseph, "Hybrid Ray-Tracing/FDTD Method for Human Exposure Evaluation of a Massive MIMO Technology in an Industrial Indoor Environment," *IEEE Access*, vol. 7, pp. 21 020–21 031, Feb. 2019.

[21] S. Y. Seidel and T. S. Rappaport, "Site-Specific Propagation Prediction for Wireless in-Building Personal Communication System Design," *IEEE Trans. Veh. Technol.*, vol. 43, no. 4, pp. 879–891, Nov. 1994.

[22] G. Durgin, N. Patwari, and T. S. Rappaport, "An Advanced 3D Ray Launching Method for Wireless Propagation Prediction," in *IEEE Vehicular Technology Conference*, vol. 2, May 1997, pp. 785–789.

[23] Z. Yun and M. F. Iskander, "Ray Tracing for Radio Propagation Modeling: Principles and Applications," *IEEE Access*, vol. 3, pp. 1089–1100, Jul. 2015.

[24] Z. Yun, M. F. Iskander, and Z. Zhang, "Fast Ray Tracing Procedure Using Space Division With Uniform Rectangular Grid," *Electron. Lett*, vol. 36, no. 10, pp. 895–897, May 2000.

[25] C.-H. Teh, B.-K. Chung, and E.-H. Lim, "An Accurate and Efficient 3-D Shooting-and- Bouncing-Polygon Ray Tracer for Radio Propagation Modeling," *IEEE Trans. Antennas Propag.*, vol. 66, no. 12, pp. 7244–7254, Dec. 2018.

[26] Z. Yun, M. F. Iskander, and Z. Zhang, "Development of a New Shooting-and-Bouncing Ray (SBR) Tracing Method That Avoids Ray Double Counting," in *IEEE Antennas and Propagation Society International Symposium*, vol. 1, Jul. 2001, pp. 464–467 vol.1.

[27] G. Carluccio, F. Puggelli, and M. Albani, "A UTD Triple Diffraction Coefficient for Straight Wedges in Arbitrary Configuration," *IEEE Trans. Antennas Propag.*, vol. 60, no. 12, pp. 5809–5817, Dec. 2012.

[28] P. H. Pathak, G. Carluccio, and M. Albani, "The uniform geometrical theory of diffraction and some of its applications," *IEEE Antennas and Propagation Magazine*, vol. 55, no. 4, pp. 41–69, 2013.

[29] R. Piesiewicz, C. Jansen, D. Mittleman, T. Kleine-Ostmann, M. Koch, and T. Kurner, "Scattering analysis for the modeling of thz communication systems," *IEEE Transactions on Antennas and Propagation*, vol. 55, no. 11, pp. 3002–3009, 2007.

[30] ITU-R, "Recommendation ITU-R P.676-13: Attenuation by Atmospheric Gases and Related Effects," ITU, Tech. Rep. P.676-13, Aug. 2022.

[31] ——, "Recommendation ITU-R P.2040-3: Effects of Building Materials and Structures on Radiowave Propagation above about 100 MHz," ITU, Tech. Rep. P.2040-3, Aug. 2023.

[32] P. M. Santos and E. N. Júlio, "A State-of-the-Art Review on Roughness Quantification Methods for Concrete Surfaces," *Construction and Building Materials*, vol. 38, pp. 912–923, 2013.

[33] E. Björnson and L. Sanguinetti, "Power Scaling Laws and Near-Field Behaviors of Massive MIMO and Intelligent Reflecting Surfaces," *IEEE Open Journal of the Communications Society*, vol. 1, pp. 1306–1324, 2020.